Analyst

ROYAL SOCIETY OF CHEMISTRY

PAPER

View Article Online
View Journal | View Issue

Open Access Article. Published on 22 2024. Downloaded on 09.02.2026 21:20:27.
This article is licensed under a Creative Commons Attribution 3.0 Unported Licence.

Check for updates

Cite this: *Analyst*, 2024, **149**, 2637

Antimicrobial effects of silver nanoparticle-microspots on the mechanical properties of single bacteria†

Giada Caniglia, *[a] Dimitrios Valavanis,[b] Gözde Tezcan,[b] Joshua Magiera,[b] Holger Barth,[c] Joachim Bansmann,[d] Christine Kranz *[a] and Patrick R. Unwin *[b]

Received 31st January 2024,
Accepted 21st March 2024

DOI: 10.1039/d4an00174e

rsc.li/analyst

Silver nanoparticles (AgNPs) conjugated with polymers are well-known for their powerful and effective antimicrobial properties. In particular, the incorporation of AgNPs in biocompatible catecholamine-based polymers, such as polydopamine (PDA), has recently shown promising antimicrobial activity, due to the synergistic effects of the AgNPs, silver(I) ions released and PDA. In this study, we generated AgNPs-PDA-patterned surfaces by localised electrochemical depositions, using a double potentiostatic method *via* scanning electrochemical cell microscopy (SECCM). This technique enabled the assessment of a wide parameter space in a high-throughput manner. The optimised electrodeposition process resulted in stable and homogeneously distributed AgNP-microspots, and their antimicrobial activity against *Escherichia coli* was assessed using atomic force microscopy (AFM)-based force spectroscopy, in terms of bacterial adhesion and cell elasticity. We observed that the bacterial outer membrane underwent significant structural changes, when in close proximity to the AgNPs, namely increased hydrophilicity and stiffness loss. The spatially varied antimicrobial effect found experimentally was rationalised by numerical simulations of silver(I) concentration profiles.

Introduction

Silver nanoparticles (AgNPs) have received significant attention due to their antimicrobial activity and relative biocompatibility, being nowadays employed in numerous daily life applications, such as food storage, textiles, medical devices, and the manufacturing industry.[1–4] Their antimicrobial effectiveness arises from the synergistic effect of the AgNPs themselves and the released silver(I) ions.[5–8] AgNPs (diameter < 50 nm) and silver(I) ions can penetrate the cell wall, leading to (i) increased levels of reactive oxygen species, (ii) disruption of DNA replication cycles, (iii) mitochondrial dysfunction, and (iv) ribosome inhibition, and thus cell inactivation and death.[5,9,10] The biocide activity of AgNPs is influenced by many factors including surface chemistry, shape and size distribution, morphology, presence of capping agents, dissolution rate, and efficiency in ion release.[11] Therefore, the fabrication of the AgNPs is an important step that must be optimised to obtain controlled nanostructures, uniform in size, morphology, and functionalities. To avoid the agglomeration of the AgNPs and control the size distribution, functional polymeric coatings with groups such as hydroquinone motifs have shown promising potential for the immobilization and stabilization of AgNPs.[12,13]

Polydopamine (PDA), a nature-inspired biopolymer, has been widely used as a coating to synthesise *in situ* AgNPs,[12,14] with promising results for the application of PDA-AgNPs as antimicrobial composite films.[15–17] Niyonshuti *et al.*, also suggested that PDA coatings may have a synergistic effect and enhance the antimicrobial activity of AgNPs.[15] Although the reductive properties of PDA, due to the presence of catechol groups, have been used to chemically synthesize AgNPs starting from dilute $AgNO_3$ solutions,[12,13] this approach is somewhat time-consuming and a controlled particle size distribution appears to be difficult to achieve in the absence of common reduction agents, such as $NaBH_4$.[18] Instead, electro-

[a]*Institute of Analytical and Bioanalytical Chemistry, Ulm University, Albert-Einstein-Allee, 11 89081 Ulm, Germany. E-mail: christine.kranz@uni-ulm.de, giada.caniglia@uni-ulm.de*
[b]*Department of Chemistry, University of Warwick, Coventry, CV4 7AL, UK. E-mail: P.R.Unwin@warwick.ac.uk*
[c]*Institute of Experimental and Clinical Pharmacology, Toxicology and Pharmacology of Natural Products, University of Ulm Medical Center, Albert-Einstein-Allee, 11 89081 Ulm, Germany*
[d]*Institute of Surface Chemistry and Catalysis, Ulm University, Albert-Einstein-Allee 47, 89081 Ulm, Germany*

† Electronic supplementary information (ESI) available. See DOI: https://doi.org/10.1039/d4an00174e

Open Access Article. Published on 22 2024. Downloaded on 09.02.2026 21:20:27.
This article is licensed under a Creative Commons Attribution 3.0 Unported Licence.

chemical methods, and in particular the double-potentiostatic method,[19] are well-established strategies that lead to a reproducible, simple, and eco-friendly synthesis of AgNPs at different conductive or semi-conductive materials.[19] According to the literature, AgNPs have mainly been electro-deposited on metal electrodes (gold and platinum)[20,21] and conducting oxides (indium tin oxide and aluminium-doped zinc oxide).[19,22,23] However, the electrochemical deposition of AgNPs onto polymeric substrates is a field still poorly explored.[24–27]

In this work, the electrodeposition of AgNPs onto PDA has been investigated, using a double-potentiostatic method *via* scanning electrochemical cell microscopy (SECCM).[28,29] We could achieve a fast optimization of the deposition process and perform screening experiments using SECCM, which is a versatile scanning probe microscopy (SPM) technique that is particularly well-suited to surface patterning *via* local electrodeposition, making use of positioning, timing, and size of the micro- or nano-electrochemical cell, defined by the size of the SECCM pipettés orifice. The setup consists of a pipette filled with an electrolytic solution and equipped with a quasi-reference counter electrode (QRCE). The pipette is approached to the sample (working electrode) until the hanging droplet (meniscus) at the end of the pipette makes contact with the surface, forming a local electrochemical cell.[29] The pipette itself does not come into contact with, or affect, the surface, rendering it a non-contact technique. In comparison to other micro-spotting techniques,[30] SECCM, and in general SPM techniques, have already shown their capacity for the potential-controlled patterned electrodeposition of polymers[31,32] and micro- and nano-metre structures[33–41] on a variety of substrates.

The generation of AgNP-microspots using SECCM brings several advantages for the deposition and analysis of antibacterial materials. Firstly, since it allows the formation of arrays of tens of spots using different experimental electrodeposition conditions, large datasets can be generated *via* SECCM in a short time. Secondly, due to the generation of circular AgNP-microspots, it is possible to study the behaviour of single bacteria as a function of the distance from the antimicrobial source. Thus, evidence of the dependence of cell attachment on silver(I) concentration can be obtained and supported by multiphysics simulation. Morphological, nanomechanical, and antimicrobial characterisation of the PDA-AgNPs-bacteria system was performed *via* atomic force microscopy (AFM)-based force spectroscopy[42] in terms of adhesion properties and bacterial elasticity as a function of the distance from the AgNP-microspots and bacteria.

Experimental

Material and chemicals

Sodium chloride (NaCl), sodium hydrogen phosphate (Na_2HPO_4), and sodium dihydrogen phosphate (NaH_2PO_4) were purchased from Merck (Germany). Dopamine hydrochloride, silver nitrate ($AgNO_3$), and potassium nitrate (KNO_3) were purchased from Sigma-Aldrich (Germany). Luria–Bertani (LB) culture medium was purchased from VWR International GmbH (Germany). All solutions were freshly prepared in ultrapure water from a Millipore Milli-Q system (resistivity: 18.0 MΩ cm at 25 °C).

Macroscale electrochemical deposition of polydopamine

Macroscopic electrochemical measurements were performed using a CHI842B bipotentiostat (CH Instruments, USA) in a three-electrode configuration with a 4 cm^2 gold-coated silicon substrate as a working electrode, a platinum counter electrode, and Ag/AgCl/KCl (sat.) reference electrode. PDA films were electrodeposited from a purged solution of 5.3 mmol L^{-1} dopamine hypochlorite in 10 mmol L^{-1} PBS buffer (pH 7.4) using pulsed electrodeposition as described elsewhere.[43,44] Briefly, PDA was pulse-deposited onto the gold working electrode by applying 25 cycles with a potential pulse sequence of +0.5 V/2 s; 0.0 V/2 s; −0.3 V/2 s; 0.0 V/3 s *vs.* Ag/AgCl/KCl (sat.). After the deposition, the PDA film was electro-oxidized in a 10 mmol L^{-1} PBS solution (pH 7.4) by applying a potential of +0.5 V for 300 s *vs.* Ag/AgCl/KCl (sat.) to ensure the oxidation of the hydroquinone groups, which might be the main responsible for the chemical reduction of silver(I) and AgNPs formation.[12]

SECCM based electrodeposition

SECCM experiments were done using a home-built setup as described elsewhere.[28,29,37] Experiment control and data collection were handled by the publicly available Warwick Electrochemical Scanning Probe Microscopy (WEC-SPM) platform,[45] running on an FPGA card (PCIe 7852R, National Instruments, Austin, USA) and a LabVIEW 2019 interface (National Instruments). Current measurements were performed using a custom-built current amplifier.

Pipette probes were prepared by pulling quartz capillaries (1.00 mm OD, 0.50 mm ID, Sutter Instruments, USA) using a laser pipette puller (P-2000, Sutter Instruments) to obtain two (sister) pipettes, each with an end diameter of 5 μm. The probes were back-filled with the chosen electrolyte solution, containing 0.05 mmol L^{-1} to 5.0 mmol L^{-1} $AgNO_3$, in 50 mmol L^{-1} KNO_3. An AgCl-coated Ag wire was inserted in the back opening of the pipette and connected as the QRCE. The prepared probe was then mounted on a linear piezoelectric actuator (P-753.3CD, Physik Instrumente, Karlsruhe, Germany) for vertical movement (z-axis) orthogonal to the PDA-coated gold substrate. The latter was mounted on a two-axis (x–y) piezoelectric actuator (P-625.2CD, Physik Instrumente) for lateral movement. The experimental setup was placed inside a Faraday cage, in turn, fixed on a vibration-dampening optical table (RS2000 and S-2000A-423.5 automatic levelling isolators, Newport, USA). The pipette was first positioned at a distance of *ca.* 50 μm from the substrate by using micro-positioners (M-461, Newport, USA), assisted by visualization with a digital camera (PL-B776U, PixeLink, Ottawa, Canada) and a cold light source (MI-150, Edmund Optics, Mainz, Germany). The automated approach of the probe was then conducted at a speed of

 This journal is © The Royal Society of Chemistry 2024

Open Access Article. Published on 22 2024. Downloaded on 09.02.2026 21:20:27.
This article is licensed under a Creative Commons Attribution 3.0 Unported Licence.

1 μm s^{-1} and while applying a potential of +0.2 V *vs.* Ag/AgCl to the (open) cell so that a surface current could be detected once the electrolyte meniscus came into contact with the surface. Upon contact and detection of the pre-set current threshold, the approach was halted, and the pipette was kept stationary for 0.01 s (waiting time), before starting the potential-induced electrodeposition. AgNPs were formed using a double-potentiostatic method, *i.e.*, by first applying a large overpotential (E_1 = −0.4 V *vs.* Ag/AgCl) for 0.5 s (first step duration, t_1); and subsequently a low overpotential (E_2 = −0.2 *vs.* Ag/AgCl) during a longer period of time (second step duration, t_2 = 1.5 s; 2.5 s; 3.5 s and 4.0 s). A primary large overpotential applied for a short time is needed for the rapid and homogeneous nucleation and growth of the AgNPs.[46] The following low overpotential – which corresponds to the electrochemical reduction of silver(I) – favours the slow growth of the formed AgNPs, inhibiting the formation of new nuclei.[19] Experiments without the application of the first potential (*i.e.*, setting t_1 = 0 s and effectively applying only the E_2 step) were also performed to investigate its influence on the size and distribution of the AgNPs. After the electrodeposition of AgNPs at each landing spot, the pipette was retracted from the surface at a speed of 2 μm s^{-1} and moved automatically to the next deposition site, at a distance defined by the experimental protocol. Data was analysed using MATLAB R2021a (Mathworks, USA) and OriginPro 2021 v. 9.8.0.200 (OriginLab Corporation, USA) software.

Bacterial culture conditions

Strains of *E. coli* DH5-α (originally obtained from Clontech Laboratories, Inc., Heidelberg, Germany) were inoculated in aerobic conditions to 100 mL of 25 g L^{-1} sterile LB medium at 37 ± 1 °C overnight, using a shaking incubator (KS 4000ic control, Keison Products, UK). The bacterial suspension was harvested and resuspended in dilute LB medium (0.5 g L^{-1}) and incubated at 37 ± 1 °C up to a concentration of 7 × 10^8 CFU mL^{-1} (OD_{600} = 0.9). The OD_{600} was monitored using a UV-Vis spectrometer (Thermo Scientific NanoDrop One, Massachusetts, USA). The bacterial culture was then seeded on the PDA-AgNP-modified substrates by immersing them into the bacterial solution and incubating at 37 ± 1 °C for 20 h. For adhesion experiments, the PDA-AgNP samples were rinsed twice with LB medium and MilliQ water and immersed in a 10 mmol L^{-1} PBS (pH 7.4) solution.

Force–distance measurements and AFM imaging

A 5500 AFM/SPM system equipped with a close-loop scanner from Keysight (Keysight Technologies, AZ, USA) was used for all AFM imaging and force spectroscopy experiments. AFM images were recorded in air in contact mode using silicon nitride probes (MLCT, Bruker AFM probes, CA, USA; nominal spring constant of 0.1 N m^{-1}) and a scan speed of 0.52 ln s^{-1}. Force–distance curves were recorded in solution (10 mmol L^{-1} PBS, pH 7.4) using silicon nitride probes (MLCT, Bruker AFM probes, CA, USA; tip radius of 20 nm and nominal spring constant of 0.1 N m^{-1}) with a loading force of 200 nN. A sweep rate of 1.0 μm s^{-1} was applied to minimize hydrodynamic effects. The actual force constants of the cantilevers were determined using the thermal noise method.[47]

Statistical analyses are based on the Student *t*-test assuming unequal variance. Data evaluation was performed using MoutainSPIP v. 9 (Digital Surf, France) and OriginPro 2021 software, v 9.8.0.200 (OriginLab Corporation).

Scanning electron microscopy

The scanning electron microscopy (SEM) characterisation was performed using either a Zeiss SUPRA 55 FE-SEM instrument (Zeiss, Germany) or a Helios NanoLab 600 FIB/SEM (ThermoFisher, the Netherlands). Images were acquired at 5.00 kV with a beam current of 86 pA. Data evaluation was performed using MoutainSPIP v. 9 (Digital Surf, France) and ImageJ v 1.54f (National Institutes of Health, USA).

Simulation model for evaluating silver(I) release

A three-dimensional finite element method (FEM) model was used for the evaluation of silver(I) concentration resulting from the dissolution of AgNPs. The selected geometric configuration consisted of a volumetric domain represented by a sufficiently large square box (10 × 10 × 10 cm^3), chosen to mitigate the impact of domain size on simulation outcomes. The lower face of the square box (referring to the sample surface) was equipped with either a singular 5 μm-diameter solid disc, serving as a representative description of AgNP deposits or an array of such discs. The adoption of a solid disc was justified by the negligible height of the deposited AgNP-spots, and the relatively large spot coverage achieved (see electron microscopy analysis below). To obtain an approximation of the silver(I) flux, we first investigated experimentally the AgNP-microspot dissolution over time. We immersed the patterned samples in LB medium (in the absence of bacteria) and recorded the change in NP size over time, *via* successive SEM imaging, obtaining a decrease in particle diameter equal to 30% after 6 hours of immersion. All computational simulations were executed utilizing the FEM software, COMSOL Multiphysics (version 6.1, COMSOL AB, Sweden) using the transport of diluted species module, with extended details presented in ESI (2): COMSOL report.†

Results and discussion

Electrochemical deposition of AgNPs

A schematic of the SECCM configuration and the steps for the AgNPs electrodeposition, *via* the double-potentiostatic method, are depicted in Fig. S1.†

SECCM is highly suitable for optimising the electrodeposition of AgNPs on PDA with respect to the experimental parameters (or variables) that could influence the size and shape distribution of the NPs, as arrays of AgNPs using different parameters can be deposited onto the same sample. By this approach, the time for optimisation can be significantly reduced and uncertainties related to variations of the substrate

Open Access Article. Published on 22 2024. Downloaded on 09.02.2026 21:20:27.
This article is licensed under a Creative Commons Attribution 3.0 Unported Licence.

(*i.e.*, variations of PDA electrodeposition) can be eliminated. Optimisation variables considered in this study include deposition times (t_1 and t_2) for each potential step, $AgNO_3$ concentration, and polymer thickness. E_1 and E_2 were fixed to E_1 = −0.4 V and E_2 = −0.2 V *vs.* Ag/AgCl. We selected a primary potential of −0.4 V for two main reasons: (i) according to previous works,[19,22] potentials from *ca.* −0.4 V are suitable for the electrodeposition of AgNPs that are homogenously distributed; and (ii) more negative potentials may affect the electrochemical and physicochemical properties of PDA.[48]

Fig. 1A shows the cyclic voltammogram obtained from a 0.5 mmol L^{-1} $AgNO_3$ solution (in 50 mmol L^{-1} KNO_3 as electrolyte), in which the two applied potentials used for the AgNPs electrodeposition are marked with the arrows. The first potential pulse was E_1 = −0.4 V, sufficient to form silver nuclei homogenously distributed at the PDA surface.[19,22] The second pulse, E_2 = −0.2 V corresponds to a potential in proximity to the formal potential of silver(I) reduction. The optimisation of the AgNPs electrodeposition involved a two-factor/three-level factorial design, *i.e.*, three different precursor concentrations ($AgNO_3$ 5.00 mmol L^{-1}, 0.50 mmol L^{-1}, and 0.05 mmol L^{-1}) and three different deposition times ($t_1 \times t_2$: 0.0 × 4.0 s; 0.5 × 3.5 s, and 0.5 × 2.5 s) were investigated. Examples of current-time curves recorded in a solution of 0.5 mmol L^{-1} $AgNO_3$ in 50 mmol L^{-1} KNO_3, with t_1 set to 0.5 or 0 s, are depicted in Fig. 1B.

Table 1 summarises the parameters used for the electrodeposition of AgNPs and the obtained average particle diameter, while Fig. 2 shows representative SEM images of the AgNP-spots electrodeposited by varying those parameters. Fig. 2A displays an SEM image of the AgNPs electrodeposited on a 25-cycle PDA film, without the application of the high overpotential step (t_1 = 0 s) and $AgNO_3$ concentration equal to 5.0 mmol L^{-1}.

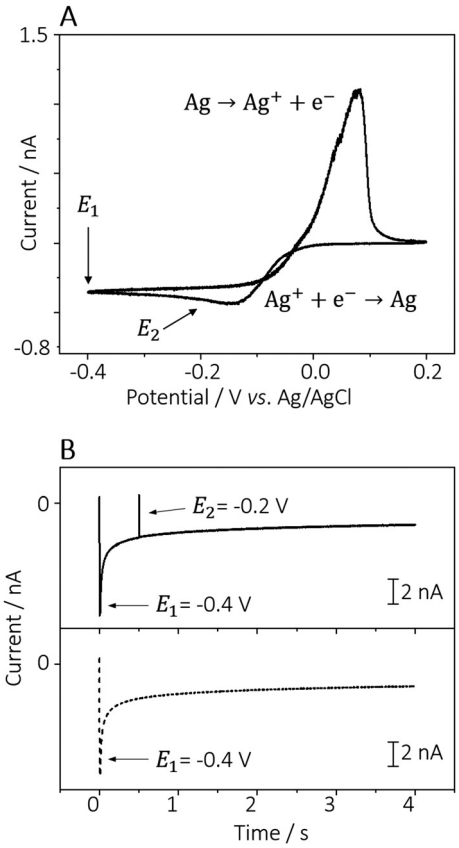

Fig. 1 (A) Cyclic voltammogram of a 0.5 mmol L^{-1} $AgNO_3$ in 50 mmol L^{-1} KNO_3 solution recorded at the PDA-modified gold electrode. The potentials applied for the electrodeposition of AgNPs (E_1 and E_2) are highlighted with black arrows. (B) Exemplary current–time curves of the electrodeposition process *via* a double (continuous line) and single (dotted line) potentiostatic step. Conditions: $AgNO_3$ concentration: 0.5 mmol L^{-1}; KNO_3 concentration: 50 mmol L^{-1}; SECCM pipette diameter: 5 μm; working electrode: PDA-modified gold electrode.

Table 1 Average particle diameter as a function of the $AgNO_3$ concentration and deposition step times. Applied potentials have been kept constant (−0.4 V and −0.2 V, respectively)

$AgNO_3$ concentration (mmol L^{-1})	t_1 (s) (E_1 = −0.4 V throughout)	t_2 (s) (E_2 = −0.2 V throughout)	AgNPs diameter[a] (nm)
5.00	0.0	4.0	171 ± 4[b]
5.00	0.5	3.5	77 ± 2
5.00	0.5	2.5	55 ± 1
0.50	0.0	4.0	159 ± 11[c]
0.50	0.5	3.5	26 ± 1
0.50	0.5	2.5	19 ± 1
0.05	0.0	4.0	22 ± 2
0.05	0.5	3.5	17 ± 2
0.05	0.5	2.5	8 ± 3

[a] n > 650 AgNPs. [b] n = 100 AgNPs. [c] n = 135 AgNPs.

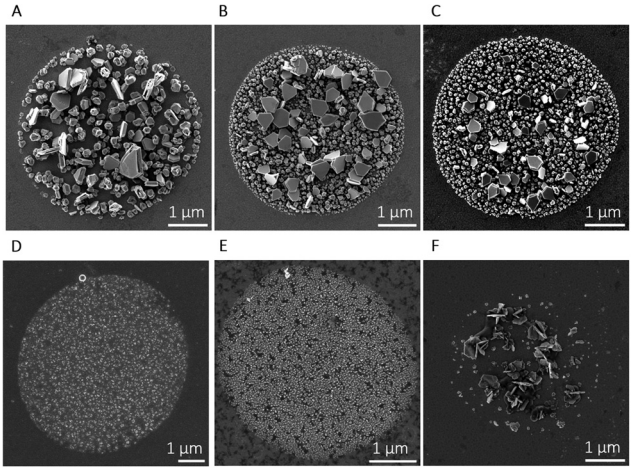

Fig. 2 Representative SEM images of AgNPs spot obtained *via* SECCM using pipettes with a diameter of ∼5 μm, on a 25-cycle PDA film. The applied potentials were kept constant (E_1 = −0.4 V and E_2 = −0.2 V *vs.* Ag/AgCl). (A) [$AgNO_3$] = 5.0 mmol L^{-1}, t_1 = 0 s, t_2 = 4.0 s; (B) [$AgNO_3$] = 5.0 mmol L^{-1}, t_1 = 0.5 s, t_2 = 3.5 s; (C) [$AgNO_3$] = 5.0 mmol L^{-1}, t_1 = 0.5 s, t_2 = 2.5 s; (D) [$AgNO_3$] = 0.5 mmol L^{-1}, t_1 = 0.5 s, t_2 = 2.5 s; (E) [$AgNO_3$] = 0.05 mmol L^{-1}, t_1 = 0.5 s, t_2 = 2.5 s; (F) [$AgNO_3$] = 5.0 mmol L^{-1}, t_1 = 0.5 s, t_2 = 2.5 s, and 50-cycle PDA film.

Open Access Article. Published on 22 2024. Downloaded on 09.02.2026 21:20:27. This article is licensed under a Creative Commons Attribution 3.0 Unported Licence.

The particles exhibit multiple shapes (truncated tetrahedral, dendritic, octahedral) and an average particle size of 171 ± 4 nm (n = 100). The particle size was evaluated without considering the larger truncated tetrahedral-shaped particles (double-hexagon-apothem = 455 ± 1 nm, n = 40). The AgNPs obtained in this way (*i.e.*, in a single potential step) were compared with the ones depicted in Fig. 2B, deposited with the same total electrodeposition time (4 s), but here utilising the double-potentiostatic method: a high overpotential pulse for 0.5 s (E_1 = −0.4 V) and a growth pulse for 3.5 s (E_2 = −0.2 V). It is evident that a short nucleation pulse results in more uniform particle sizes and distribution. Indeed, the particles shown in Fig. 2B and C grew more homogeneously over the entire surface in which the meniscus was formed.

However, the relatively long growth time also favours the formation of larger truncated twinned tetrahedral AgNPs with an average size equal to 448 ± 26 nm (calculated as the double apothem of the hexagonal particle, n = 9). By maintaining a constant precursor concentration of 5.0 mmol L^{-1} and a first pulse of 0.5 s at −0.4 V, the particle size decreased significantly from 77 ± 2 nm (n = 501) to 55 ± 1 (n = 492) when the growth time was decreased by 1 s (as shown in Fig. 2B and C). At lower silver(I) ion concentrations, *i.e.*, 0.50 mmol L^{-1} (Fig. 2D) and 0.05 mmol L^{-1} (Fig. 2E), the particle size decreased further and AgNPs grew homogeneously in size and shape, due to the lower concentration of silver(I). As shown in Table 1 the particle size distribution at different $AgNO_3$ concentrations drops to 19 ± 1 nm (0.5 mmol L^{-1}, n = 1012) and 8 ± 3 nm (0.05 mmol L^{-1}, n = 1748). These depositions were carried out at deposition times of t_1 = 0.5 s and t_2 = 2.5 s, respectively.

The influence of the PDA film thickness on the electrodeposition of AgNPs was also investigated by electrodepositing AgNPs on a thicker layer of PDA, as obtained by a 50-cycle pulsed-deposition (*ca.* 3–4 nm film thickness) instead of a 25-cycle (*ca.* 1–2 nm film thickness).[39] Fig. 2C and F show the electrodeposition of AgNPs on 25-cycle-PDA and 50-cycle-PDA, respectively, with all the other optimisation parameters being kept the same: $AgNO_3$ concentration 5.0 mmol L^{-1}; t_1 = 0.5 s (E_1 = −0.4 V); growth time t_2 = 2.5 s (E_2 = −0.2 V). As shown in Fig. 2F, the electrodeposition of AgNPs onto a thicker polymeric layer (50-cycle-PDA) was not favourable, with the formation of small, dispersed particles and larger polyhedral and dendritic-shaped AgNPs. The imperfect electrodeposition of AgNPs onto a thicker PDA film might be due to a decreased electron transfer rate through the polymer, as reported by Kund *et al.*[43] in their work using scanning electrochemical microscopy.

Antimicrobial studies

To screen the antimicrobial effects, we designed arrays of AgNP-microspots so that the behaviour of multiple sets of bacteria could be investigated on the same sample. We focused on the behaviour of the bacteria *E. coli* in the initial stage of cell attachment by studying the variation of the adhesion forces and elasticity using AFM-based force spectroscopy (AFM-FS).

The antimicrobial activity of the AgNPs was tested using the particles obtained with the following optimised parameters: (i) concentration of $AgNO_3$ of 0.05 mmol L^{-1}; (ii) first potential step equal to −0.4 V *vs.* Ag/AgCl applied for 0.5 s, and (iii) second potential step equal to −0.2 V *vs.* Ag/AgCl applied for 2.5 s. Under these conditions, a particle size of 8 ± 3 nm (n = 1748) was obtained. This size of AgNPs fits the optimal range since AgNPs with a diameter up to 50 nm exhibit increased stability, biocompatibility, and enhanced antimicrobial activity.[10]

Even so, the AgNPs were deposited *via* an electrochemical method in electrolytic solutions without any capping agent, we expect the AgNPs to be comprised of silver(0) forming stable complexes with the quinone functional groups of the PDA.[49] However, the coordination with PDA might not be sufficient to favour the spontaneous oxidative dissolution of the AgNPs to release silver(I) ions, decreasing the antimicrobial effect of the AgNPs.[50] Indeed, as shown in the SEM images depicted in Fig. S2A and B,† when the as-prepared AgNPs-PDA sample is inoculated in *E. coli* cultures for 20 h, bacteria appear to be unaffected by the presence of the AgNPs, even attaching near and on top of the AgNP-spots. Since no silver(I) is expected to be released from the AgNPs, longer inoculation times might be needed to observe the antimicrobial effect.

To promote AgNP dissolution, the AgNPs-PDA samples were treated with UV-ozone for 30 minutes, in order to oxidize the surface of the AgNPs to form silver oxide. The presence of a layer of silver oxide around the metallic AgNPs promotes dissolution, firstly of the oxide and subsequently of the metallic silver.[51,52] The SEM images shown in Fig. S2C and D,† demonstrate the antimicrobial effect of the treated AgNPs-PDA samples. The amount of bacteria attached on the surface is strongly decreased when compared to bacteria in contact with PDA only (no AgNPs present, Fig. S2E†), or with untreated AgNPs-PDA (Fig. S2A and B†). Indeed, while the surface coverage on the bare PDA or in the presence of untreated AgNPs was, respectively, 16 ± 1% and 11 ± 1%; after the treatment of the AgNPs with UV/ozone, the bacterial coverage dropped down to 3.0 ± 0.3% (Fig. S3†). The coverage was evaluated by the study of three different 100 × 100 μm^2 SEM images from different samples.

The oxidation of silver(0) to silver(I) was confirmed by X-ray photoelectron spectroscopy (XPS) measurements obtained from untreated and UV-ozone-treated samples recorded in the range from 378 eV to 364 eV. The chemical state of the AgNPs was determined by the position of the peaks at 374.4 eV and 368.4 eV associated with the binding energy of the emitted. The XPS spectrum of the untreated AgNPs (Fig. 3A, blue line) shows peaks at 374.4 eV (Ag $3d_{3/2}$) and 368.4 eV (Ag $3d_{5/2}$) revealing that the dominant state of the untreated AgNPs is metallic.[53] The XPS spectrum of the UV-ozone treated AgNPs (red line in Fig. 3A) shows the two peaks shifted to lower binding energies (374.1 eV and 368.1 eV respectively), proving the presence of oxidized AgNPs.[53] The XPS survey spectra (1400 eV to 0 eV) of the untreated and treated samples are shown in Fig. S4.†

Open Access Article. Published on 22 2024. Downloaded on 09.02.2026 21:20:27.
This article is licensed under a Creative Commons Attribution 3.0 Unported Licence.

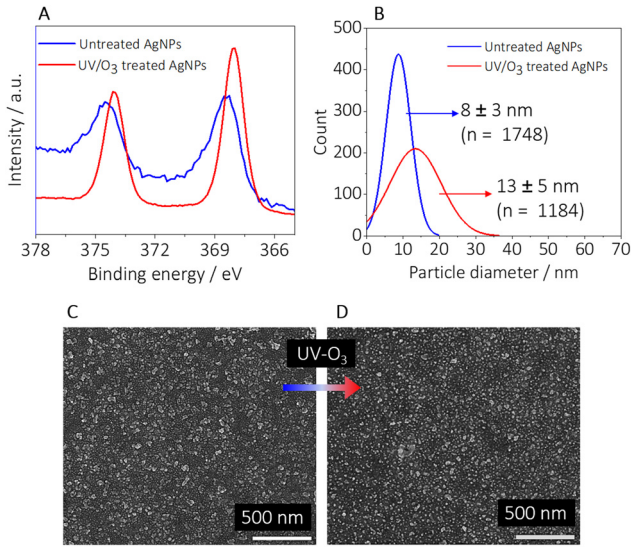

Fig. 3 (A) XPS high-resolution spectra of Ag $3d_{3/2}$ and Ag $3d_{5/2}$ from the untreated (blue line) and UV/ozone treated (red line) AgNPs-PDA samples. (B) Size distribution of the AgNPs before (blue line) and after (red line) the treatment with UV-ozone. (C and D) Representative SEM images of AgNPs (C) before and (D) after UV-ozone treatment. The NPs were deposited on PDA with the following parameters: E_1 = −0.4 V, E_2 = −0.2 V *vs.* Ag/AgCl, t_1 = 0.5 s, t_2 = 2.5 s, and [$AgNO_3$] = 0.5 mmol L^{-1}.

The change in the size of the AgNPs after the treatment with UV-ozone (Fig. 3B–D) is associated with the formation of a thin oxide layer around the NPs. The size of the particles increased to diameters more than 45% larger (Fig. 3B) compared to the untreated particles.

To investigate the antimicrobial effect of the oxidized AgNPs, morphological and nanomechanical studies of individual *E. coli* cells were performed *via* AFM and AFM-FS. The bacterial cells were inoculated on the ozone-treated AgNPs-PDA samples. As shown in Fig. 4A, isolated bacteria are visible in the proximity of the AgNP-spot (at a distance of 2–5 μm), while at larger distances from the AgNPs (Fig. 4B), where the flux of silver(I) ions released is expected at a lower rate, bacteria form small communities of about tens of cells (blue arrows in Fig. 4B).

High-resolution AFM images displayed in Fig. 4C and D clearly show that bacteria attached at a short distance from the AgNP-spot exhibit changes in their morphology with reduced cell size and the appearance of corrugations and grooves on the cell surface. These characteristics can be correlated to the disruption of the outer membrane (OM) due to the exposure to silver(I) ions released from the AgNP-spot. This behaviour is consistent with previous observations in other Gram-negative bacterial strains in contact with silver(I) ions[8] or hostile environments.[54]

The deformation of the outer cell membrane due to the presence of the AgNPs might also change the nanomechanical properties of the bacterial surface. One of the antimicrobial pathways of the AgNPs (and, synergistically, the silver(I) ions) derives from the high affinity of silver(I) with sulphur-containing proteins.[10] Two of the most important sulphur-containing proteins in *E. coli* are the so-called RcsF and Nlpe.[55] These are outer membrane lipoproteins whose main function is monitoring the integrity of the OM. Although the mechanism of action of AgNPs through RcsF and Nlpe is still not well understood, recent studies have shown that the inactivation or alteration of these lipoproteins, *e.g.*, by antimicrobials, leads to the inhibition of the peptidoglycan synthesis and production of capsular oligosaccharides, which in turn results in the deformation or disruption of the OM.[50] These changes in the conformation and composition of the OM might affect both the hydrophobicity and the stiffness of the bacterial OM. To prove this assumption, we investigated the adhesion force and Young's modulus of bacteria grown at tens of micrometres away (Fig. 4A), and in proximity (Fig. 4B), of the AgNP-microspots.

Force–distance curves recorded on cells attached in the proximity of the AgNP-microspots revealed lower adhesions forces (0.4 ± 0.1 nN, n = 424 recorded force curves on 7 cells) in comparison to cells grown at a distance larger than 20 μm from the spots (1.2 ± 0.3 nN, n = 388 recorded force curves on 9 cells), as shown in Fig. 4E. We attribute this change in adhesion to an increase in the hydrophilicity of the bacterial OM due to the release of silver(I) ions. This behaviour suggests that there is a profound change in the OM composition produced by the AgNPs and the silver(I) ions released from the NPs.

It is generally accepted that the hydrophilicity of *E. coli* arises from the contribution of the hydrophilic C–O and C–N functional groups associated with polysaccharides and the C–C and C–H hydrophobic functional groups of hydrocarbons.[56] However, the interaction of the silver(I) ions from the AgNPs with the OM of *E. coli* affects the sulphur-containing membrane lipoproteins that control the integrity of the OM.[10,55] When perturbed, these lipoproteins modulate the formation of higher amounts of capsular oligosaccharides to stabilize the cell membrane.[55] Due to the presence of a higher concentration of oligosaccharides with hydrophilic character, an increase in the hydrophilicity of the bacterial cell is expected, and thus a smaller adhesion force is recorded by the hydrophobic Si_3N_4 AFM probe.

The results pertaining to the elasticity (Fig. 4F) of the bacteria are in accordance with the assumption that the cells directly exposed to AgNPs suffer from changes and disruption of the OM. The elasticity is correlated to Youngs modulus (E_S), calculated from the force–distance curves using the Hertz model for the fitting.[57,58] The cells directly exposed to the AgNPs are less stiff (E_S = 10 ± 1 MPa, n = 450 recorded force curve on 7 cells) than the cells at a distance of more than 20 μm from the spots (E_S = 22 ± 2 MPa, n = 428 recorded force curve on 9 cells). Recent studies[59] showed that bacteria grown in healthy conditions exhibit stiff OM due to the presence of structural molecules such as lipopolysaccharides and that the integrity and rigidity of the membrane are directly correlated to the cell mechano-sensitivity: *i.e.*, a tension sensor that plays an important role in the osmoregulation of the bacteria. Accordingly, other works have suggested[60,61] that one of the

 This journal is © The Royal Society of Chemistry 2024

Open Access Article. Published on 22 2024. Downloaded on 09.02.2026 21:20:27.
This article is licensed under a Creative Commons Attribution 3.0 Unported Licence.

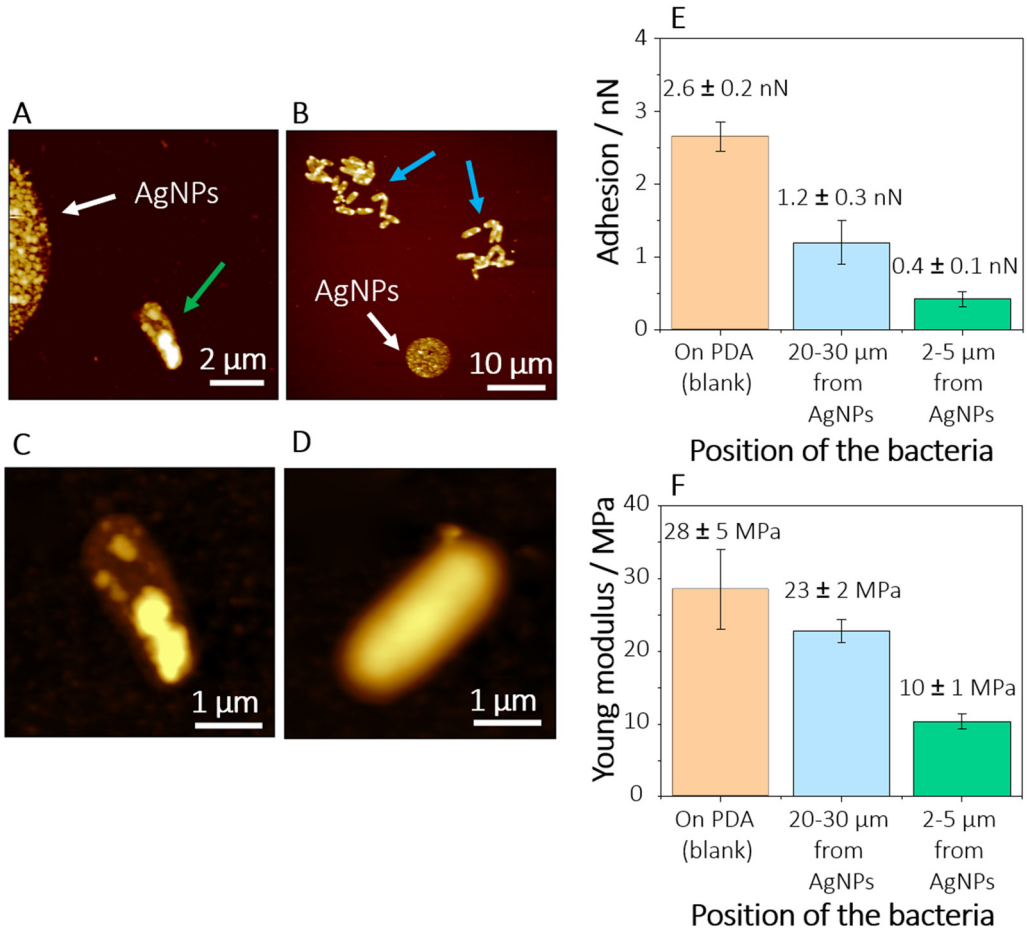

Fig. 4 (A and B) AFM topography images recorded in air of *E. coli* inoculated on ozone-treated AgNP-PDA samples. (A) Single cell (green arrow) attached to the surface in the proximity of the AgNP-microspot. (B) Overview of small communities of bacteria (blue arrows) attached to the sample surface, at more than 20 µm from the AgNPs spot. High-resolution images of a single cell (C) attached in the proximity (2–5 µm) of the AgNPs spot and (D) attached more than 20 µm from the AgNPs spot. (E and F) Bar charts of the measured (E) adhesion forces and (F) Young's modulus at single bacteria. Error bars reflect the measurements of at least 7 bacterial cells and 380 force curves. ANOVA statistical tests show that there is a significant difference in the adhesion and elasticity properties of bacteria as a function of the distance to the microspot, in which the bacteria attached (null hypothesis rejected).

contributions of the OM stiffness is related to the ionic bonds between the lipopolysaccharides. The interaction of their negatively charged moieties with cationic ions disrupts these bonds, leading to an alteration of the lipid packing and thus a decrease in stiffness.[62] A loss of rigidity in cells exposed to AgNPs and silver(I) ions might be then due to the interaction and chelation of silver(I) with the lipopolysaccharides and the consequent rupture of the lipidic ionic bonds, OM corrugation, and cell lysis.

Worth mentioning is the comparison of the bacterial nanomechanical properties of cells attached in an environment with the presence of silver(I) ions and cells that proliferated in an Ag-free environment, where only PDA was present. Even though bacteria attached more than 20 µm away from the AgNP-spot exhibit a smooth morphology (Fig. 4D), characteristic of healthy cells, they also exhibit higher hydrophilicity and loss of stiffness in comparison to bacteria grown in an Ag-free environment (Fig. 4E and F). The determined adhesion force and elasticity of cells attached to pure PDA films exhibit slightly larger values in comparison to bacteria attached in the presence of AgNPs, being 2.7 ± 0.2 nN (n = 517 recorded force curves on 11 cells) and 28 ± 5 MPa (n = 517 recorded force curves on 11 cells), respectively. ANOVA statistical tests (significance level α = 0.05) show that there is a significant difference in the nanomechanical properties of bacteria (adhesion and elasticity) as a function of the position in which the bacteria attached. The pairings considered were between (i) the bacteria in Ag-free environment, and the ones at 20–30 µm from AgNPs (p-value equal to 0.0001 for both adhesion and elasticity); and (ii) the bacteria in Ag-free environment, and the ones at 2–5 µm from AgNPs (p-value equal to 0.0001 for both adhesion and elasticity) – null hypothesis rejected in both cases.

Simulation studies

Since the antimicrobial properties of the AgNPs arise mainly from the release of silver(I) ions, FEM simulations were per-

Open Access Article. Published on 22 2024. Downloaded on 09.02.2026 21:20:27.
This article is licensed under a Creative Commons Attribution 3.0 Unported Licence.

formed to provide an insight into the concentration profile of silver(I) in the AgNP-spot system (see the Experimental section for a description of the observations of AgNP dissolution from the patterned samples, that informed the simulations).

The studies show that the concentration of silver(I) ions decreases monotonically from the centre of the spot, suggesting a maximum silver(I) concentration in the nanomolar range (Fig. 5). At the same immersion time, simulations reveal that from a distance of 2 μm to 20 μm the concentration of silver(I) drops by one order of magnitude (Fig. 5B). Although the concentration of silver(I) at the centre of the spots and a few micrometres away is 2 orders of magnitude lower than the minimum inhibitory concentration of silver(I) for *E. coli*,[63] any cumulative effect of the silver(I) release is not considered. Thus, the uptake of silver(I) by the bacteria over time (as compared to the instantaneous concentration referenced above) may have a significant effect, as observed in the experiments.

Moreover, recent studies demonstrated the high influence of the presence of chloride, which can inhibit or enhance the dissolution rate of AgNPs and thus the antimicrobial effect, depending on the Cl/Ag ratio. According to Levard *et al.*,[64] at lower Cl/Ag ratios (*i.e.*, Cl/Ag lower than ~10^4), the presence of chloride leads to the formation of an AgCl layer on the AgNPs which attenuates the dissolution of the particles. However, at higher Cl/Ag concentrations, the dissolution of the AgNPs might be enhanced with the formation of soluble $AgCl_x^{(x-1)-}$ species, which might also have antimicrobial effects. In the presented experiments, bacteria were growing in LB medium with a chloride concentration of 10^{-3} mol L^{-1}. Considering that a single AgNP-spot contains an average of 4×10^4 individual NPs with a diameter of *ca.* 13 nm (Fig. 3B) reflecting *ca.* 7×10^4 atoms of silver, the possible concentration of silver(I) released (assuming a total dissolution of the NPs) in the 500 μL bacterial solution was *ca.* 8×10^{-8} mol L^{-1}. Thus, the Cl/Ag ratio under the experimental conditions was *ca.* 10^5, a value in which, according to literature, the formation of $AgCl_x^{(x-1)-}$ species might be favoured, and the antimicrobial effect of the AgNP-spot enhanced. The calculation of the concentration of silver, in the context of the Cl/Ag ratio, has been explained in more detail in the ESI (section S5).†

Considering the above-mentioned aspects, the silver(I) release obtained from the simulations can be correlated to the observed behaviour of the bacteria. Indeed, as shown in Fig. 5A and B, the concentration of silver(I) close to the spot (2–5 μm away) might be high enough to affect bacteria attaching at this distance, producing a significant silver(I) intake that can lead to the disruption of the bacterial cell wall, as observed by the AFM studies (Fig. 4D). The concentration of silver(I) is expected to decrease exponentially from the AgNP-spot, thus the bacteria attached at a larger distance from the silver(I) source would be affected with reduced intensity due to the diminishing concentration levels.

For the optimisation studies performed *via* SECCM, arrays of 4 × 4 AgNP-microspots with a distance from each spot equal to 100 μm were produced. To exclude the interference of neighbouring AgNP-microspots on the concentration profile of silver (I), FEM simulations using a 4 × 4 AgNP-microspots array were carried out. Fig. 5C shows the concentration profile of silver(I) released from each spot in the array. It is worth mentioning that, by comparing the simulations obtained using as a model a single spot (Fig. 5B) and an array of spots (Fig. 5D), no significant difference in silver(I) concentration has been detected. Thus, the study of bacterial behaviour up to a distance of *ca.* 50 μm from a single AgNP-spot can be considered to be affected only by the single AgNP-microspot and the influence from the surrounding microspots can be neglected.

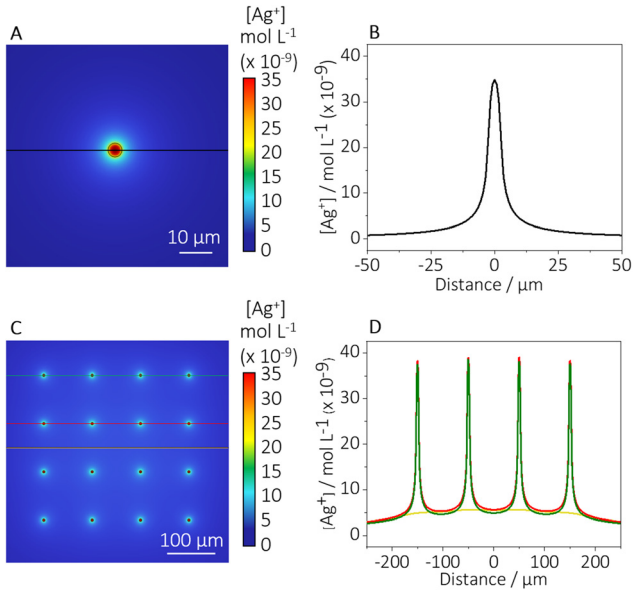

Fig. 5 FEM simulation of an electro-deposited AgNP-microspot. Graphical representation of the concentration profile of silver(I) released from (A) a single AgNPs spot and (C) an 4 × 4 array of AgNP-spots after 4 hours of immersion. (B) Concentration profile of the silver(I) released from a single AgNP spot. (D) Concentration profile of the silver(I) released from different regions of a 4 × 4 array of AgNP-spots. The colour-line in the graph corresponds to the region highlighted in (C). COMSOL report can be found in the ESI (2): COMSOL report.†

Conclusions

SECCM was employed for the electro-deposition of antimicrobial AgNP-microspots on PDA films using a double-potentiostatic method. The electrodeposition protocol has been optimised to obtain uniform depositions with AgNP sizes and shapes with a high antimicrobial performance. The influence of parameters such as nucleation time, growth time, and $AgNO_3$ concentration has been investigated, leading to an optimised protocol for the formation of AgNPs with a particle size of 8 ± 3 nm. Subsequent UV-ozone treatment was applied for the efficient release of silver(I), whose local concentration at the NP-spots was rationalised using numerical simulation. The antimicrobial activity of the ozone-treated AgNPs-PDA composites has been evaluated against *E. coli* by AFM-SF. The determined bacterial adhesion and elasticity properties indicate

 This journal is © The Royal Society of Chemistry 2024

Open Access Article. Published on 22 2024. Downloaded on 09.02.2026 21:20:27.
This article is licensed under a Creative Commons Attribution 3.0 Unported Licence.

that the envelope of *E. coli* exhibits enhanced hydrophilicity and loss of stiffness when bacteria are in close proximity (2–5 μm) to the AgNPs related to the detrimental effect on the *E. coli* OM integrity. The study highlights the antimicrobial properties of patterned AgNPs-PDA surfaces and the way they can be readily produced *via* SECCM.

Author contributions

Giada Caniglia: Conceptualisation, data curation, writing, review, and editing. Dimitrios Valavanis and Gözde Tezcan: Conceptualisation and data curation. Joshua Magiera: Numerical simulation and data curation. Holger Barth: Resources, provision of biological material. Joachim Bansmann: XPS experiments and data curation. Christine Kranz and Patrick R. Unwin: Supervision, review, and editing. All authors have approved the final version of the manuscript.

Conflicts of interest

The authors declare no competing interests.

Acknowledgements

The authors acknowledge the FIBCenter and Dr Gregor Neusser (Institute of Analytical and Bioanalytical Chemistry, Ulm University) and Dr Enrico Daviddi (Department of Chemistry, University of Warwick) for the SEM measurements. This work is part of the "Break Biofilms" project that has received funding from the European Union's Horizon 2020 research and innovation program under the Marie Skłodowska Curie Grant Agreement No. 813439. D. V. and P. R. U. acknowledge the financial support from the European Union's Horizon 2020 Research and Innovation Programme under the Marie Skłodowska Curie Grant Agreement No. 812398 ("SENTINEL" project), and from the United Kingdom's Engineering and Physical Sciences Research Council for funding under Grant EP/R018820/1 ("Crystallisation in the Real World").

References

1 M. E. Quadros and L. C. Marr, *Environ. Sci. Technol.*, 2011, **45**, 10713–10719.
2 J.-H. J. S. Kim, E. Kuk, K. N. Yu, J.-H. J. S. Kim, S. J. Park, H. J. Lee, S. H. Kim, Y. H. Y. K. Park, Y. H. Y. K. Park, C.-Y. Hwang, Y.-K. Kim, Y.-S. Lee, D. H. Jeong and M.-H. Cho, *Nanomedicine*, 2007, **3**, 95–101.
3 B. Nowack, H. F. Krug and M. Height, *Environ. Sci. Technol.*, 2011, **45**, 1177–1183.
4 X. Chen and H. J. Schluesener, *Toxicol. Lett.*, 2008, **176**, 1–12.
5 S. Tang and J. Zheng, *Adv. Healthcare Mater.*, 2018, **7**, e1701503.
6 N. Durán, M. Durán, M. B. de Jesus, A. B. Seabra, W. J. Fávaro and G. Nakazato, *Nanomedicine*, 2016, **12**, 789–799.
7 S. Agnihotri, S. Mukherji and S. Mukherji, *RSC Adv.*, 2014, **4**, 3974–3983.
8 G. Caniglia, M. C. Sportelli, A. Heinzmann, R. A. Picca, A. Valentini, H. Barth, B. Mizaikoff, N. Cioffi and C. Kranz, *Anal. Chim. Acta*, 2022, **1212**, 339892.
9 K. B. Holt and A. J. Bard, *Biochemistry*, 2005, **44**, 13214–13223.
10 T. C. Dakal, A. Kumar, R. S. Majumdar and V. Yadav, *Front. Microbiol.*, 2016, **7**, 1831.
11 X.-F. Zhang, Z.-G. Liu, W. Shen and S. Gurunathan, *Int. J. Mol. Sci.*, 2016, **17**, 1534.
12 D. Wang, L. Bao, H. Li, X. Guo, W. Liu, X. Wang, X. Hou and B. He, *Nanoscale*, 2022, **14**, 6212–6219.
13 J. Lu, J. Fang, J. Li, C. Wang, Z. He, L. Zhu, Z. Xu and H. Zeng, *ACS Appl. Nano. Mater.*, 2020, **3**, 156–164.
14 A. GhavamiNejad, L. E. Aguilar, R. B. Ambade, S.-H. Lee, C. H. Park and C. S. Kim, *Colloid Interface Sci. Commun.*, 2015, **6**, 5–8.
15 I. I. Niyonshuti, V. R. Krishnamurthi, D. Okyere, L. Song, M. Benamara, X. Tong, Y. Wang and J. Chen, *ACS Appl. Mater. Interfaces*, 2020, **12**, 40067–40077.
16 T. Wang, Wusigale, D. Kuttappan, M. A. Amalaradjou, Y. Luo and Y. Luo, *Adv. Compos. Hybrid Mater.*, 2021, **4**, 696–706.
17 J. Xu, N. Xu, T. Zhou, X. Xiao, B. Gao, J. Fu and T. Zhang, *Surf. Coat. Technol.*, 2017, **320**, 608–613.
18 A. Kumar, B. Mishra and B. P. Tripathi, *Nano-Struct. Nano-Objects*, 2020, **23**, 100489.
19 J. C. Bian, Z. Li, Z. D. Chen, H. Y. He, X. W. Zhang, X. Li and G. R. Han, *Appl. Surf. Sci.*, 2011, **258**, 1831–1835.
20 K. Fajerwerg, V. Ynam, B. Chaudret, V. Garçon, D. Thouron and M. Comtat, *Electrochem. Commun.*, 2010, **12**, 1439–1441.
21 D. Ibañez, D. Izquierdo, C. Fernandez-Blanco, A. Heras and A. Colina, *J. Raman Spectrosc.*, 2018, **49**, 482–492.
22 D. Zhang, Y. Tang, F. Jiang, Z. Han and J. Chen, *Appl. Surf. Sci.*, 2016, **369**, 178–182.
23 D. A. Crespo-Yapur, A. S. Elizondo, D. Herrera and M. Videa, *Mater. Today: Proc.*, 2022, **48**, 1–4.
24 T. Makowski, D. Kowalczyk, W. Fortuniak, S. Brzezinski and D. Kregiel, *Cellulose*, 2015, **22**, 3063–3075.
25 B.-A. Zhao, W.-F. Cai, K.-B. Pu, J.-R. Bai, J.-Y. Gao and Y.-H. Wang, *RSC Adv.*, 2022, **12**, 21793–21800.
26 A. Alqudami, S. Annapoorni, P. Sen and R. S. Rawat, *Synth. Met.*, 2007, **157**, 53–59.
27 J. Pan, Z. Zhang, Z. Zhan, Y. Xiong, Y. Wang, K. Cao and Y. Chen, *Carbohydr. Polym.*, 2020, **242**, 116391.
28 C. L. Bentley, M. Kang and P. R. Unwin, *Curr. Opin. Electrochem.*, 2017, **6**, 23–30.
29 N. Ebejer, A. G. Güell, S. C. S. Lai, K. McKelvey, M. E. Snowden and P. R. Unwin, *Annu. Rev. Anal. Chem.*, 2013, **6**, 329–351.
30 C. A. Gunawan, M. Ge and C. Zhao, *Nat. Commun.*, 2014, **5**, 3744.

Open Access Article. Published on 22 2024. Downloaded on 09.02.2026 21:20:27.
This article is licensed under a Creative Commons Attribution 3.0 Unported Licence.

31 E. E. Oseland, Z. J. Ayres, A. Basile, D. M. Haddleton, P. Wilson and P. R. Unwin, *Chem. Commun.*, 2016, **52**, 9929–9932.
32 B. D. B. Aaronson, J. Garoz-Ruiz, J. C. Byers, A. Colina and P. R. Unwin, *Langmuir*, 2015, **31**, 12814–12822.
33 P. Ciocci, D. Valavanis, G. N. Meloni, J. Lemineur, P. R. Unwin and F. Kanoufi, *ChemElectroChem*, 2023, **10**, e202201162.
34 Md. M. Rahman, C. L. Tolbert, P. Saha, J. M. Halpern and C. M. Hill, *ACS Nano*, 2022, **16**, 21275–21282.
35 H. Lee, K. C. Matthews, X. Zhan, J. H. Warner and H. Ren, *ACS Nano*, 2023, **17**, 22499–22507.
36 M. Bernal, D. Torres, S. S. Parapari, M. Čeh, K. Ž. Rožman, S. Šturm and J. Ustarroz, *Electrochim. Acta*, 2023, **445**, 142023.
37 S. C. S. Lai, R. A. Lazenby, P. M. Kirkman and P. R. Unwin, *Chem. Sci.*, 2015, **6**, 1126–1138.
38 S. Sarkar, A. C. Herath, D. Mukherjee and D. Mandler, *Electrochim. Acta*, 2022, **429**, 140986.
39 S. Sarkar and D. Mandler, *ChemElectroChem*, 2017, **4**, 2981–2988.
40 E. Oswald, K. Palanisamy and C. Kranz, *Curr. Opin. Electrochem.*, 2022, **34**, 100965.
41 F. Li, M. Edwards, J. Guo and P. R. Unwin, *J. Phys. Chem. C*, 2009, **113**, 3553–3565.
42 J. W. Goss and C. B. Volle, *ACS Appl. Bio Mater.*, 2020, **3**, 143–155.
43 J. Kund, S. Daboss, T. M. D'Alvise, S. Harvey, C. V. Synatschke, T. Weil and C. Kranz, *Nanomaterials*, 2021, **11**, 1964.
44 S. Daboss, J. Lin, M. Godejohann and C. Kranz, *Anal. Chem.*, 2020, **92**, 8404–8413.
45 Warwick Electrochemical Scanning Probe Microscopy (WEC-SPM) platform, **https://warwick.ac.uk/electrochemistry/wec-spm**, (accessed January 2024).
46 R. M. Penner, *J. Phys. Chem. B*, 2002, **106**, 3339–3353.
47 J. L. Hutter and J. Bechhoefer, *Rev. Sci. Instrum.*, 1993, **64**, 1868–1873.
48 H. Khezraqa, S.-A. Safavi-Mirmahalleh, H. Roghani-Mamaqani and M. Salami-Kalajahi, *J. Energy Storage*, 2024, **79**, 110170.
49 N. P. Shumbula, S. S. Nkabinde, Z. B. Ndala, S. Mpelane, M. P. Shumbula, P. S. Mdluli, Z. Njengele-Tetyana, P. Tetyana, T. Hlatshwayo, M. Mlambo and N. Moloto, *Arabian J. Chem.*, 2022, **15**, 103798.
50 B. Reidy, A. Haase, A. Luch, K. Dawson and I. Lynch, *Materials*, 2013, **6**, 2295–2350.
51 D. C. Choo and T. W. Kim, *Sci. Rep.*, 2017, **7**, 1696.
52 X. Li, J. J. Lenhart and H. W. Walker, *Langmuir*, 2012, **28**, 1095–1104.
53 V. K. Kaushik, *J. Electron Spectrosc. Relat. Phenom.*, 1991, **56**, 273–277.
54 E. Cefalì, S. Patanè, A. Arena, G. Saitta, S. Guglielmino, S. Cappello, M. Nicolò and M. Allegrini, *Scanning*, 2006, **24**, 274–283.
55 J.-F. Collet, S.-H. Cho, B. I. Iorga and C. V. Goemans, *J. Biol. Chem.*, 2020, **295**, 11984–11994.
56 F. Hamadi, H. Latrache, H. Zahir, A. Elghmari, M. Timinouni and M. Ellouali, *Braz. J. Microbiol.*, 2008, **39**, 10–15.
57 J. L. Alonso and W. H. Goldmann, *Life Sci.*, 2003, **72**, 2553–2560.
58 H. Hertz, *J. Reine Angew. Math.*, 1882, **92**, 156–171.
59 F. Xue, C. D. Cox, N. Bavi, P. R. Rohde, Y. Nakayama and B. Martinac, *Biochim. Biophys. Acta, Biomembr.*, 2020, **1862**, 183203.
60 R. T. Coughlin, A. A. Peterson, A. Haug, H. J. Pownall and E. J. McGroarty, *Biochim. Biophys. Acta, Biomembr.*, 1985, **821**, 404–412.
61 E. R. Rojas, G. Billings, P. D. Odermatt, G. K. Auer, L. Zhu, A. Miguel, F. Chang, D. B. Weibel, J. A. Theriot and K. C. Huang, *Nature*, 2018, **559**, 617–621.
62 K. H. Jacobson, I. L. Gunsolus, T. R. Kuech, J. M. Troiano, E. S. Melby, S. E. Lohse, D. Hu, W. B. Chrisler, C. J. Murphy, G. Orr, F. M. Geiger, C. L. Haynes and J. A. Pedersen, *Environ. Sci. Technol.*, 2015, **49**, 10642–10650.
63 E. Selem, A. F. Mekky, W. A. Hassanein, F. M. Reda and Y. A. Selim, *Saudi J. Biol. Sci.*, 2022, **29**, 103457.
64 C. Levard, S. Mitra, T. Yang, A. D. Jew, A. R. Badireddy, G. V. Lowry and G. E. Brown, *Environ. Sci. Technol.*, 2013, **47**, 5738–5745.

 This journal is © The Royal Society of Chemistry 2024